ACS Energy LETTERS

http://pubs.acs.org/journal/aelccp

LETTER

Nonfullerene Self-Assembled Monolayers As Electron-Selective Contacts for *n-i-p* Perovskite Solar Cells

Drajad S. Utomo,[⊥] Lauryna M. Svirskaite,[⊥] Adi Prasetio, Vida Malinauskiene, Pia Dally, Erkan Aydin, Artem Musiienko,* Vytautas Getautis, Tadas Malinauskas,* Randi Azmi,* and Stefaan De Wolf*

Cite This: *ACS Energy Lett.* 2024, 9, 1682−1692

Read Online

ACCESS | Metrics & More | Article Recommendations | Supporting Information

ABSTRACT: Organic, nonfullerene semiconductors capable of self-assembly and composed of either anthraquinone (AQ) or naphthalenediimide (NDI) central fragments have been designed as electron-selective materials for *n-i-p* perovskite solar cells (PSCs). Both types of self-assembled monolayer (SAM) molecules contain phosphonic acid as an anchoring group, allowing covalent binding with indium tin oxide (ITO) surfaces. In particular, the NDI-based SAMs showed a more homogeneous anchoring on the ITO substrate and a stronger band bending at the ITO-SAM/perovskite interface than AQ-based SAMs. As a result, low-temperature-processed *n-i-p* PSCs with NDI SAMs as an electron-selective bottom contact showed a maximum power conversion efficiency (PCE) of 21.5%, representing the highest PCE among *n-i-p* PSCs with organic electron transporting layers (ETLs). In addition, our NDI-SAM-based devices demonstrate substantially improved long-term stability under operating temperature conditions when compared to devices using SnO_2 as the ETL.

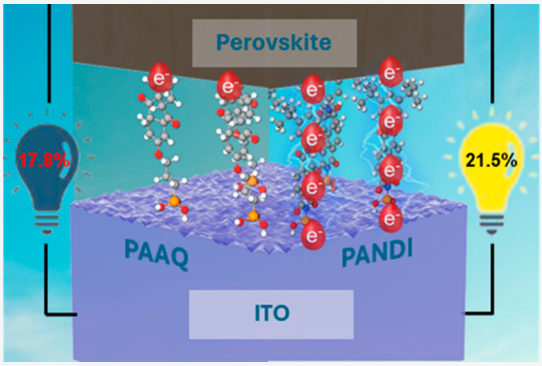

Self-assembled monolayers (SAMs) have recently emerged as a viable replacement for traditional charge transport layers in perovskite solar cells (PSCs).[1−6] In particular, SAM molecules based on carbazole and phosphonic acid groups, usually referred to as *n*PACz, where *n* is the aliphatic chain length, have attracted great interest as hole-selective contacts.[1,2,7−10] The carbazole group has a strong electron-donating moiety and thus hole-selective properties when in contact with a semiconductor, while the phosphonic acid group can covalently bond on transparent conducting oxide (TCO) surfaces to form a monolayer.[1,2,4,9,10] Thanks to their fast hole extraction and the good electronic passivation of the SAMs/perovskite interface, *p-i-n* single-junction perovskite and monolithic perovskite/silicon tandem solar cells have achieved impressive certified power conversion efficiencies (PCEs) already above 26% and 33%, respectively.[3,10−13] While new SAMs are being intensely investigated toward efficient hole collection for a range of perovskite photoabsorbers with different bandgaps, reports toward the design of novel electron-selective SAM molecules remain rare.[2,14,15] Arguably, this is due to the relative scarcity of suitable electron acceptors that are available for the synthesis of electron-selecting materials, and the required efforts toward identification and application of nonfullerene derivatives as electron-selective materials in PSCs.[16,17] Generally, the class of organic electron transport layers (ETLs) is dominated by fullerene derivatives, including C_{60} and its functionalized analogues (e.g., $PC_{61}BM$, $PC_{71}BM$, ICBA, etc.).[16−20] Nonetheless, the application of fullerene-based ETLs for solution processing is limited by the poor solubility of unmodified fullerenes in organic solvents. Moreover, synthesizing and purifying modified fullerenes, particularly C_{70} derivatives, are challenging, necessitating complex and costly multistage processes.[16,18,21]

As a nonfullerene alternative, naphthalenediimide (NDI)-based small molecules offer favorable ETL properties, such as a high electron affinity, electron mobility, and photochemical stability, coupled with simple synthesis procedures, which motivates the design of new electron-selective NDI SAMs.[22−24] Initially, NDI SAMs such as *N,N′*-bis(1-*n*-hexylpyridinium-4-ylmethyl)-1,4,5,8-naphthalenetetracarboxy-

Received: January 30, 2024
Revised: March 2, 2024
Accepted: March 6, 2024

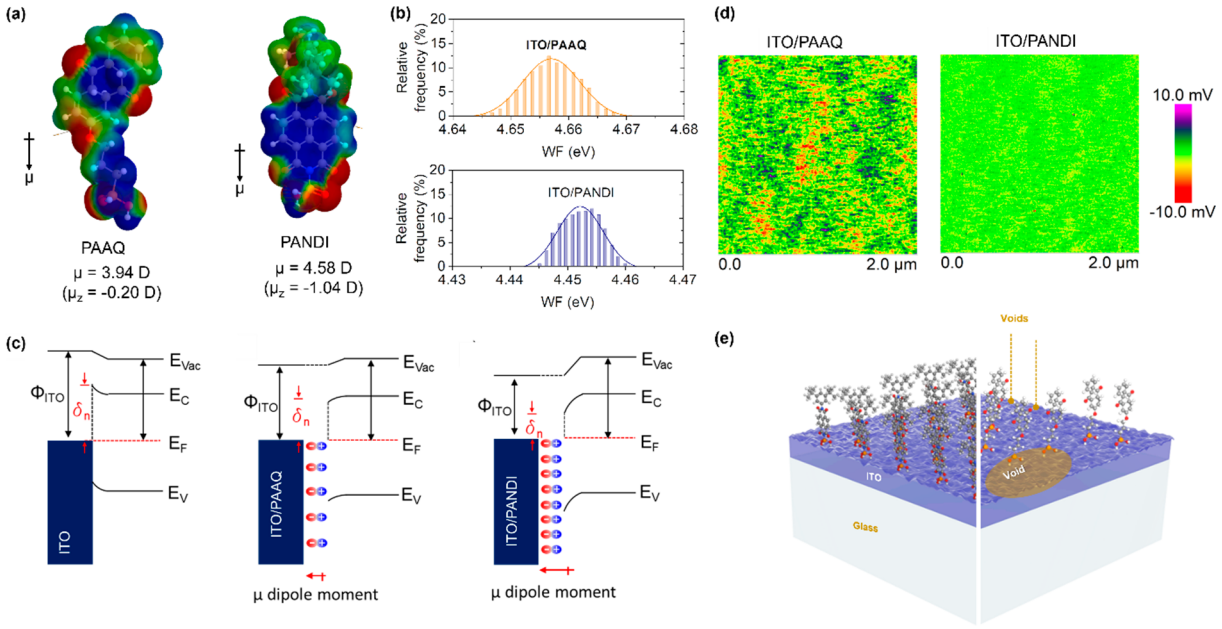

Figure 1. (a) Electrical dipole moment of PAAQ and PANDI single molecules. (b) WF histogram of ITO/PAAQ and ITO/PANDI structures. (c) Band matching of pristine ITO/perovskite, ITO/PAAQ/perovskite, and ITO/PANDI/perovskite junctions, respectively. (d) Flattened KPFM mapping images of ITO/PAAQ and ITO/PANDI films. The scale of the image ranges was normalized from −10 to 10 mV. (e) Illustration of SAM homogeneity on the ITO surface.

diimide and ammonium-bearing NDI polymers were applied as an interlayer between $PC_{61}BM$ and the metal electrode at the top contact to improve the performance of *p-i-n* PSCs.[22,25,26] Later, NDI SAMs, containing a carboxylic anchoring group, were applied directly onto indium tin oxide (ITO) substrates to lower their work function, enabling the collection of electrons in *n-i-p* PSCs.[15] These NDI-based devices demonstrated a PCE of 16% with a fill factor (FF) of 70%. Whereas these results show potential, they lag behind the best performances of regular *n-i-p* PSCs, relying typically on metal oxide ETLs (such as mesoporous TiO_2 or planar SnO_2).[27] To narrow this discrepancy in device performance mandates further improvements in electron-selective NDI SAMs.

In the search for other options for electron-selective SAMs, anthraquinone (AQ) derivatives may also be considered. The AQ structure contains two electron-accepting carbonyl functional groups, which can increase the electron affinity and are easily tunable via molecule engineering and has been reported previously as an ETL in organic solar cells (OSCs).[28,29] In recent work, the AQ derivative 1-((3-(dimethylamino)propyl)-amino)anthracene-9,10-dione was utilized in OSCs as an interface-modification layer of SnO_2, improving the conductivity of the electron-selective contact stack and improving the energy level alignment with the organic photoactive layers.[28] The resulting devices showed a PCE of 18.1%, which is among the highest values reported for *n-i-p* OSCs.[30] Inspired by these results, we explore here how the AQ moiety can also be a promising candidate toward electron-selective SAMs in *n-i-p* PSCs.

We first introduce our modification of NDI and AQ SAMs, functionalized with a phosphonic acid group to anchor directly onto ITO, toward energetic matching with the perovskite. We then investigate their use as an alternative to conventional metal oxide (i.e., TiO_2, SnO_2, and ZnO) ETLs in *n-i-p* PSCs. Contrasting with conventional processed metal oxide ETLs that usually require a higher temperature processing (≥150 °C), these new electron-selective SAMs are solution processable and only require moderate temperatures (typically up to 100 °C), which can be of benefit for certain applications, such as those relying on temperature-sensitive substrates.[31−34] Moreover, conventional solution-processed metal oxide ETLs usually require additional surface modifications with organic or inorganic materials to minimize interfacial charge losses, adding complexity toward the scalability of PSCs.[35] Here, we systematically investigated the SAMs' chemical and physical properties, including the energetic alignment and the electron extraction properties, at the ITO-SAM/perovskite interface, the materials' thermal stability, the surface wettability of ITO/SAM films, and their influences on perovskite crystallization. Finally, we fabricated *n-i-p* devices obtaining a champion PCE of 21.5%, representing the highest PCEs among *n-i-p* PSCs with organic ETLs. We also tested the operational stability of our SAM-based devices at 65 °C with above 90% retention of their initial performance for 1000 h.

The synthesis routes of *N*-(2,5-di-*tert*-butylphenyl)-*N*′-(methyl)-1,4,5,8-naphthalene tetracarboxylic diimide phosphonic acid (**PANDI**) and {3-[(9,10-dioxo-9,10-dihydroanthracen-2-yl)oxy]propyl} phosphonic acid (**PAAQ**) are shown in Scheme S1. The reaction conditions and detailed synthetic procedures are discussed in the Supporting Information (SI). These results were confirmed by using nuclear magnetic resonance (NMR) analysis, as shown in Figures S1−S8. Cyclic voltammetry (CV) and thermogravimetric analysis (TGA) were conducted to understand our SAMs' electrochemical and thermal stability properties. The redox potential from CV determines the highest occupied molecular orbital (HOMO) and lowest unoccupied molecular orbital (LUMO) energy levels of **PANDI**- and **PAAQ**-based SAMs. Note that these values do not represent absolute solid-state electron affinities or ionization energies but can be used to make relative comparisons between the different compounds. The voltammograms of **PANDI** and **PAAQ** in solution show reversible

https://doi.org/10.1021/acsenergylett.4c00306
ACS Energy Lett. 2024, 9, 1682−1692

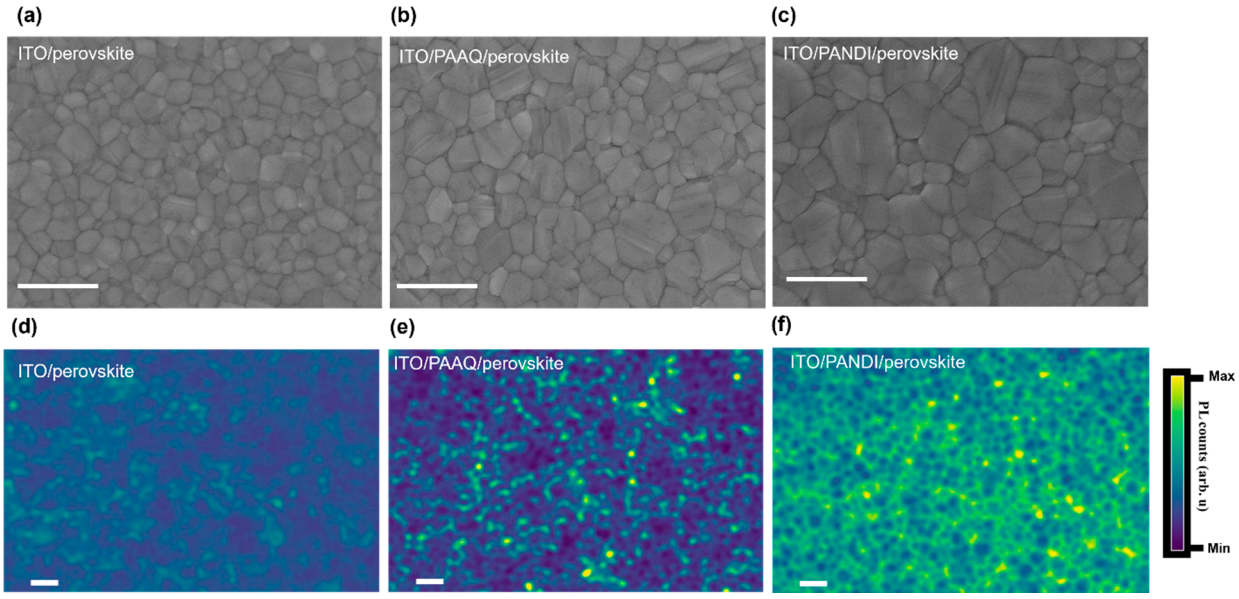

Figure 2. (a–c) Top view of SEM images of perovskite on the bare-ITO, ITO/PAAQ, and ITO/PANDI surfaces, respectively, with a scale bar of 1 μm. (d–f) Normalized hyperspectral mapping of the perovskite surface on bare-ITO, ITO/PAAQ, and ITO/PANDI with a scale bar of 2 μm.

reduction waves during the scans and are typical for NDI and AQ derivatives (see Figure S9a). The reversible process indicates that both materials exhibit good electrochemical stability. The calculated energy level redox potential measurements result in E_{LUMO} = −3.81 and −3.52 eV while E_{HOMO} = −6.97 and −6.79 eV, respectively, for **PANDI** and **PAAQ** (summarized in Table S1). Both materials demonstrate good E_{LUMO} alignment with the conduction band minima (CBM) of the perovskite absorbers, while the E_{HOMO} energy levels are sufficiently high with reference to the valence band maxima (VBM) to block holes from the perovskite layer. In addition, both SAM molecules also provide good thermal and optical properties. For instance, TGA measurements prove that **PANDI** and **PAAQ** SAM molecules are sufficiently thermally stable with only 5% weight loss at 356 and 268 °C, respectively (Figure S9b). Furthermore, UV–vis transmittance results of SAM functionalization on the ITO surface show negligible optical losses compared to bare ITO and ITO/SnO_2 films (see Figure S10).

To gain a better understanding of how SAMs anchoring affects the work function (WF) of the ITO substrate, we also conducted calculations on the electric dipole moments of each SAM molecule in the gas phase (Figure 1a). Accordingly, we found that the net dipole moment of **PAAQ** at 3.94 D is smaller than that of **PANDI** (4.58 D). However, it is crucial to acknowledge that the net dipole moments of SAM molecules may not linearly follow the WF values, as the orientation and packing of the SAMs with respect to the ITO surface is still not fully understood.[36,37] Nevertheless, by assuming the perpendicular orientation of the SAM molecules to the substrates, the *z*-projection of the dipole moment becomes particularly relevant, given its higher contribution compared to the *x*- and *y*-projections. Upon calculation, we found that the *z*-projection dipole moment values for **PAAQ** and **PANDI** are −0.20 and −1.04 D, respectively (Figure S11 and Table S2). It is worth noting that while assuming a perpendicular orientation of **PAAQ** and **PANDI** to the surface, the presence of long alkyl chains connecting phosphonic acid and anthraquinone in **PAAQ** may cause slight tilting of the SAMs. The negative sign indicates that the negative pole is directed toward the phosphonic acid anchoring group. The higher value of the dipole moment will enhance the WF of ITO to align better with the CBM of perovskite.

We then obtained the WF of the ITO/SAM samples from the contact potential difference (CPD; the detailed calculation is given in the SI) that was obtained by scanning Kelvin probe force microscopy (KPFM), as shown in Figure 1b and Figure S12. The WF of ITO/**PANDI** (∼4.45 eV) is found to be lower than that of ITO/**PAAQ** (∼4.66 eV), indicating a more favorable energetic alignment for electron extraction. Therefore, the larger WF difference of ITO/**PANDI** (∼0.27 eV) than ITO/**PAAQ** (∼0.10 eV), in reference to bare-ITO, enhances the band bending at the ITO/**PANDI**/perovskite interface, thereby improving its electron selectivity (see also the schematic illustration in Figure 1c).[38,39] The larger shift of the WF of **PANDI** can be associated with its larger interface dipole compared to **PAAQ**, as discussed above.[40−42] Apart from WF modifications, the SAM coatings do not significantly change the surface roughness of ITO, as shown by AFM results in Figure S13.

We also analyzed the chemical composition on the surface to understand the anchoring and coverage of SAM molecules on ITO by performing X-ray photoelectron spectroscopy (XPS; see Figure S14 and Table S3). Quantifying the surface coverage was also possible by calculating the presence of carbon (C 1s) and indium (In $3d_{5/2}$) in different positions across the sample area. This approach can determine the concentration of hydrogen bonding between SAMs and phosphonic acid attached to the indium-based substrate. The ratio P/In shows a high lateral variation in the surface region of **PAAQ** compared to **PANDI** on the ITO substrate (Tables S4 and S5). This analysis, therefore, provides a comprehensive picture of the electronic property dependence on the surface homogeneity. In addition, Figure 1d shows a surface mapping of CPD values of SAMs on ITO to further experimentally verify the uniformity of the SAM coverage. The more

https://doi.org/10.1021/acsenergylett.4c00306
ACS Energy Lett. 2024, 9, 1682−1692

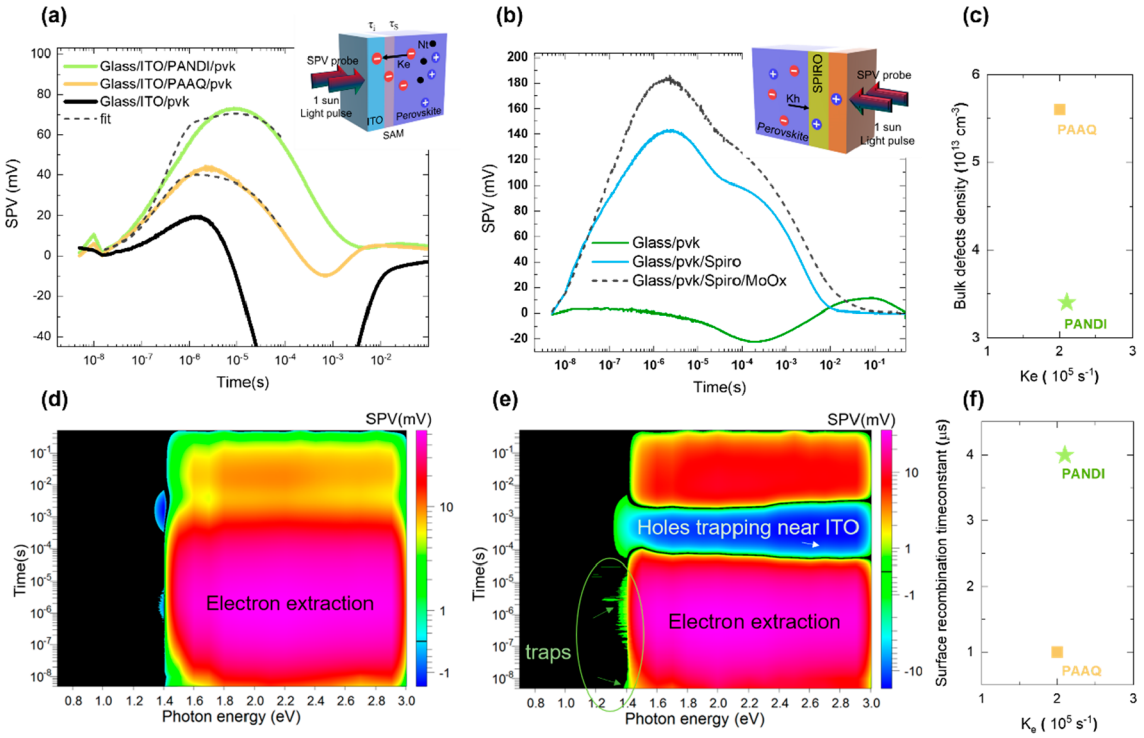

Figure 3. (a, b) Charge extraction dynamics generated from trSPV measurements for ETL and HTL stack. (c) Bulk defect density. trSPV spectra from (d) PANDI and (e) PAAQ. (f) Surface recombination time constant defining how fast free carriers recombine near the perovskite surface.

homogeneous pattern is proportional to the absence of WF fluctuations in a specific area. This shows that the ITO/**PANDI** interface has a narrower WF distribution than the ITO/**PAAQ** case, indicating a better **PANDI** coverage on ITO as illustrated in Figure 1e, in accordance with the XPS results.

The coated **PANDI** molecules onto ITO significantly increase ITO's surface hydrophobicity to a contact angle of around 78.4° versus **PAAQ**-coated ITO and bare ITO, with values of around 42.2 and 28.5°, respectively (Figure S15). It is noted that all of the samples were washed with chlorobenzene or methanol to remove unbound SAM molecules from the ITO substrate. This reveals that only SAMs attached onto ITO will affect the surface hydrophobicity that can be directly associated with our SAMs' coverage on ITO.[43] The higher surface hydrophobicity of the ITO/SAM substrate will affect the crystallization and morphology of the perovskite film.[39,44] The more hydrophobic (i.e., less wetting) surface of the ITO/**PANDI** case can enhance the surface mobility of the perovskite inks, resulting in larger-grain-size perovskite crystals, as indicated from top-view scanning electron microscopy (SEM) images in Figure 2a−c.[39,44,45] In addition, the functional head methyl group at **PANDI** can interact well with the perovskite layer, resulting in fewer pinholes or voids formed at the ITO/**PANDI**/perovskite interface (see the cross-sectional SEM image in Figure S16).[3,4] In contrast, the poor contact can result in some voids at the ITO/perovskite and ITO/**PAAQ**/perovskite bottom interface.

Next, we investigate the perovskite quality film via steady-state photoluminescence (PL) and time-resolved PL decay measurements. The steady-state PL intensity of the perovskite film coated on ITO/**PANDI** surfaces achieves a higher PL intensity than the ITO- and ITO/**PAAQ**-based samples (Figure S17a). This improvement is consistent with the increased carrier lifetime of the ITO/**PANDI**/perovskite sample ($\tau_{average}$ of 3.1 μs) compared to the ITO/**PAAQ**/perovskite sample ($\tau_{average}$ of 2.2 μs), extracted from time-resolved PL measurements (Figure S17b). A larger perovskite crystal grain size implies a decrease of the relative amount of grain boundaries, directly reducing nonradiative recombination.[39,44] To visualize how the SAMs influence the perovskite film quality, confocal microscopy and local PL mapping of perovskite films was performed. Figure 2d−f shows hyperspectral PL microscopy images of the corresponding microscopy images above (Figure 2a−c) and corresponds to wavelengths emitted at 798 nm. We investigated the local distribution of PL on a microscale at the perovskite film surface.[46] This local PL distribution is correlated to the perovskite film quality, which is depicted through a color gradation from black to light yellow. For the ITO/perovskite sample, a lower PL emission spectrum is observed, indicated by a darker region, while the ITO/**PAAQ**/perovskite sample exhibits a higher PL emission but with a large spatial variation. Interestingly, the ITO/**PANDI**/perovskite sample has fewer local spatial variations with a stronger emission, indicating a higher perovskite film quality.[46,47]

To demonstrate the charge extraction capabilities at the ETL/perovskite and perovskite/HTL interfaces, we utilized the transient surface photovoltage (trSPV) with a 5 ns laser pulse and 1 sun equivalent fluence, as shown in Figure 3a,b. Generally, the trSPV signal is directly proportional to the concentration of extracted carriers, thereby providing a maximum signal amplitude and signal rise time, which offer qualitative information on the effectiveness of charge transport. Both SAMs exhibit positive signals, indicating efficient electron extraction (Figure 3a). Among them, **PANDI** demonstrated a larger amplitude and a faster rise time. The initial spike may be

https://doi.org/10.1021/acsenergylett.4c00306
ACS Energy Lett. 2024, 9, 1682−1692

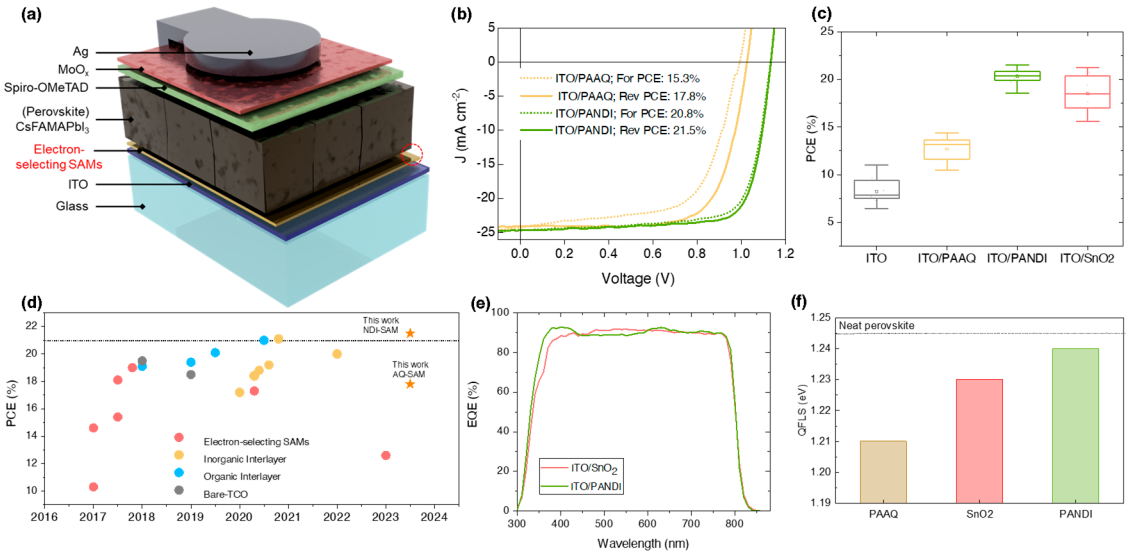

Figure 4. (a) Device scheme of employed *n-i-p* PSCs with electron-selective SAM. (b) Representative *J*−*V* characteristics of PAAQ and PANDI under the forward and reverse scan directions. (c) PCE statistics for bare-ITO-, ITO/PAAQ-, ITO/PANDI-, and ITO/SnO_2-based PSCs, respectively. (d) Summary of device efficiency of electron-selective SAMs and ETL-free *n-i-p* devices from the literature. (e) EQE spectra of ITO/SnO_2- and ITO/PANDI-based devices. (f) QFLS values of perovskite film with different ETLs.

attributed to the transfer of a small fraction of hot carriers to the SAM. Notably, the ITO/perovskite interface exhibited a negative signal after 4 μs, likely associated with free hole trapping or accumulation near the ITO interface. A similar behavior was observed for **PAAQ**, most probably induced by direct contact between ITO/perovskite due to the nonuniform coverage of **PAAQ** SAMs onto ITO, causing the trSPV signal to represent the superposition of electron extraction (6 ns to 4 μs) and hole trapping (4 μs to 10 ms). In contrast to electron extraction, the hole extraction by spiro-OMeTAD displayed a larger amplitude and a faster rise time (Figure 3b), indicating that the ETL/perovskite interface is a charge extraction bottleneck in the devices. It is noted that an additional MoO_x layer can slightly enhance the hole extraction capabilities at the perovskite/spiro-OMeTAD/MoO_x top contact stack.

We then simulated charge transport, using a model based on rate equations (eq 1), to provide a quantitative understanding of the charge extraction and the defect activation energies. Our model accounts for nonradiative recombination channels in the bulk and at the surfaces, characterized by the defect concentration in the bulk (N_t) and time constants responsible for surface and interface recombination (τ_s and τ_i, respectively). The trSPV signal is given by eq S7. The dynamics of the electron concentration decay is given by the equation

$$\frac{dn}{dt} = -K_{e\_ETL}n + K_{eb\_ETL}n_{ETL} - C_b(np) - n\sigma_{et}v_e(N_t - n_t) - \frac{n}{\tau_s} \quad (1)$$

where K_{e_ETL} and K_{eb_ETL} are electron rate constants for the extraction/injection of electrons from/to the perovskite, respectively. n and p are the photoinduced electron and hole densities, respectively. C_b, σ_e, and v_e are the radiative recombination constant, electron capture cross-section of the charge trap, and the thermal velocity of electrons, respectively, taking values from previous work.[8] We then determined the charge transport constants by fitting our model to the experimental data, using K_{e_ETL}, N_t, τ_s, and τ_i as fitting parameters (dashed line in Figure 3a,b), shown in Table S6. The charge extraction rate constant showed a comparable value for both SAMs (Figure 3c).

To investigate the defect activation energies in the perovskite, we measured trSPV with a tunable wavelength laser with photon energies in the range of 0.7−3 eV, as shown in Figure 3d,e. The perovskite deposited on **PAAQ** exhibited clear signals below the bandgap, indicating charge accumulation due to the presence of a deep defect. In addition, the ITO/**PAAQ**/perovskite film also displayed a signature of hole trapping, demonstrated by the blue region in the SPV dynamics. In contrast, the ITO/**PANDI**/perovskite film displayed negligible signals below the bandgap and for hole trapping. As a result, perovskites deposited on **PANDI** showed a marked lower defect density (3.4×10^{13} cm^{-3}) compared to the **PAAQ** (5.6×10^{13} cm^{-3}), highlighting the beneficial role of **PANDI** in improving the electronic quality of the perovskite film (see Table S7).[8] Additionally, **PANDI** significantly suppressed surface and interface recombination by a factor of 4 (Figure 3f).[48,49] Furthermore, the capabilities of SAM in passivating surface and bulk defects, particularly through crystallization modification, resulted in better performance of the solar cell devices, as discussed below. The reported time constants are in agreement with trPL data in Figure S17b and previous reports for high-quality perovskite thin films.[50−52]

We then evaluated the performance of the **PAAQ** and **PANDI** SAMs on ITO as electron-selective materials at the bottom contact of *n-i-p* PSCs, with spiro-OMeTAD as HTL in the top contact (see Figure 4a). Following our previous work, we applied a 2D perovskite passivation treatment on top of perovskite films to improve the overall device performance and stability.[9] As shown in Figure S18, the absence of an electron-selective SAM layer on ITO leads to a high surface recombination at the bottom contact, limiting the device performance to a PCE of only 11.9%.[8,53] In contrast, insertion of the **PAAQ** and **PANDI** SAMs between the ITO/perovskite interface—besides enhancing the electron selectivity of the

https://doi.org/10.1021/acsenergylett.4c00306
ACS Energy Lett. 2024, 9, 1682−1692

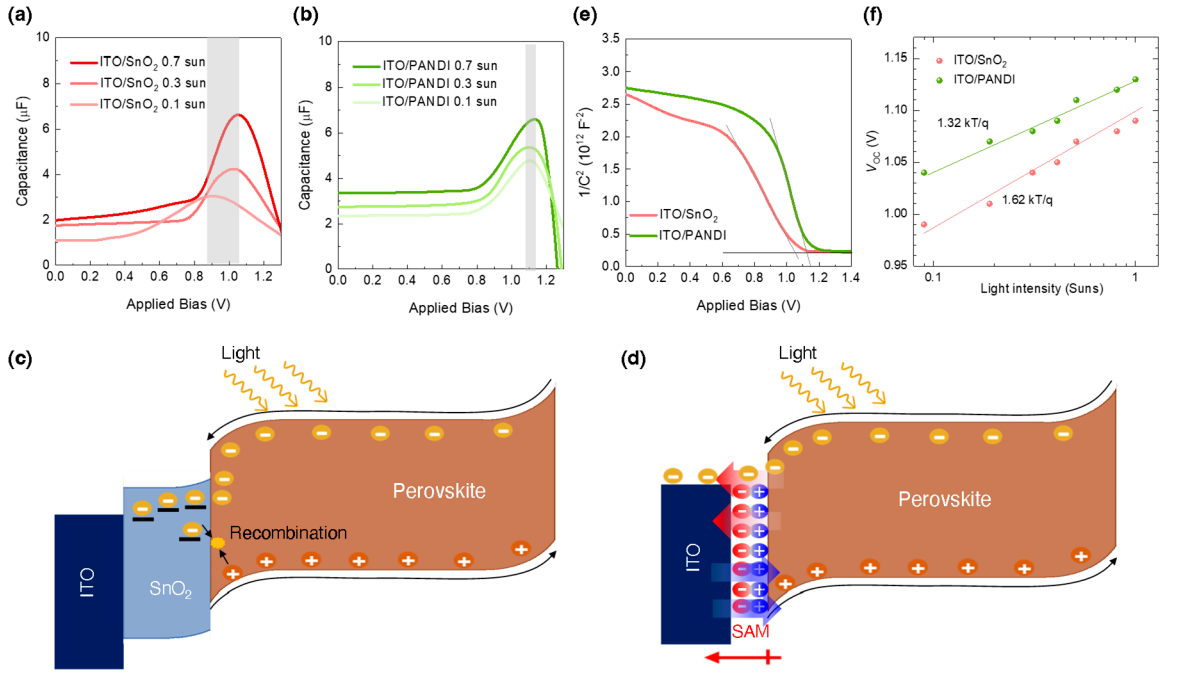

Figure 5. Photoassisted capacitance−voltage of different devices: (a) SnO_2 and (b) PANDI. (c, d) Illustration of trap charge at interface of pristine SnO_2 and SAM based devices, respectively. (e) Mott−Schottky plot and (f) V_{OC} with respect to light intensity of devices based on SnO_2 and PANDI ETLs.

bottom contact—could suppress this type of recombination by repelling holes due to the strong internal electric field at the interface.[19,39,54] As a result, **PAAQ**-based devices show an increase in performance with a maximum PCE of 17.8% (V_{OC} of 1.03 V, J_{SC} of 24.1 mA cm^{-2}, FF of 72%; Figure 4b). Despite this improvement over the SAM-free reference device, **PAAQ**-based devices feature limited V_{OC} and FF values, which could be due to the low surface coverage of **PAAQ** on ITO, resulting in unfavorable electronic properties and a lesser perovskite quality, as discussed above.

The **PANDI** SAM shows a more homogeneous coverage on ITO, with a higher surface dipole, enhancing the band bending and suppressing surface recombination effectively.[14,41] As a result, **PANDI**-based devices exhibit a higher device performance with a maximum PCE of 21.5% (V_{OC} of 1.13 V, J_{SC} of 24.7 mA cm^{-2}, FF of 77%) under a reverse scan with a negligible hysteresis. This result is among the highest reported for electron-selective SAMs and ETL-free based *n-i-p* PSCs (see Table S8 and Figure 4d). The statistical distribution of our electron-selective SAMs from 25 devices is shown in Figure 4c and Figure S18, which, with its narrower PCE distribution, shows the reproducibility of our **PANDI**-based devices. We also fabricated *n-i-p* PSCs with pristine SnO_2 as the ETL for comparison, resulting in a PCE of ∼21.2% (comparable to that in the literature; Figure S19).[32,33,55,56] In addition, the application of **PANDI** SAMs was further explored for flexible substrates, giving a PCE of 17.7% (Figure S20a,b). This outcome underscores the use of SAMs in accommodating substrates that require lower-temperature processing. The successful implementation of PANDI SAMs on ITO-PET highlights its potential for improving the performance of emerging technologies reliant on a flexible and low-temperature substrate (Table S9).[57,58]

Figure 5e shows the external quantum efficiency (EQE) of the **PANDI**- and SnO_2-based devices. Interestingly, the EQE of the **PANDI**-based device exhibits a slightly higher overall J_{SC} than SnO_2-based devices because of a higher absorption in the blue part of the spectrum, likely due to the lower optical reflectance losses of ITO/**PANDI** structures, as mentioned above. We also calculated the quasi-Fermi-level splitting (QFLS) from absolute PL measurements by using a calibrated 532 nm excitation laser at ∼1 sun condition to understand the correlation to the V_{OC} improvement of our devices (Figure 4f). Notably, ITO/**PANDI**/perovskite samples show the highest QFLS value of around 1.24 eV compared to the ITO/SnO_2/perovskite (1.23 eV)- and ITO/**PAAQ**/perovskite-based (1.21 eV) samples. The higher QFLS value on the **PANDI** indicates effective suppression of nonradiative recombination at the electron-selective buried interface.[59] This highlights how our **PANDI**-SAM yields lower optical reflectance and energetic losses, simultaneously, compared to the conventionally used SnO_2 ETL.

To evaluate charge extraction (accumulation/trapping) at the device level, we measured photoassisted capacitance−voltage ($C-V$).[60,61] Figure 5a,b shows the $C-V$ characteristics for **PANDI** and pristine SnO_2 ETL based devices under different light intensities. Interestingly, the change in peak potential (V_{peak}) under reverse bias as the function of different light intensities is correlated with interfacial charge accumulation.[60,61] The SnO_2-based device shows a significant V_{peak} shift due to interfacial charge trapping, as illustrated in Figure 5c. In contrast, due to a higher internal electric field from the dipole moment of SAM, the **PANDI**-based device exhibits a marginal V_{peak} shifting, indicating negligible charge accumulation (Figure 5d).[14,37,39,41,60,62−64] The reduced charge accumulation also resulted in a negligible photocurrent hysteresis in **PANDI**-based devices. Further, the enhanced built-in potential (V_{bi}) values of **PANDI**-based devices extracted from Mott−Schottky plots correspond to the shallower WF of ITO/**PANDI** and a higher electric dipole of the SAM (Figure 5e). As a result, the higher V_{bi} can be

https://doi.org/10.1021/acsenergylett.4c00306
ACS Energy Lett. 2024, 9, 1682−1692

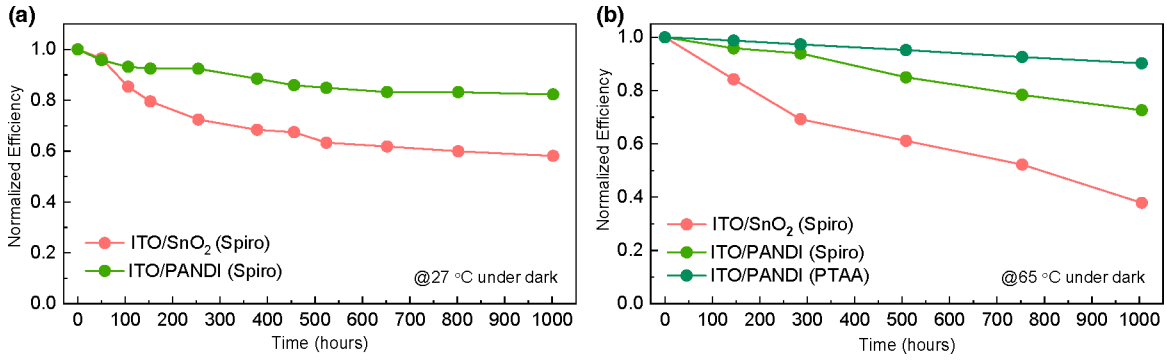

Figure 6. Evolution of normalized PCEs for nonencapsulated devices based on SnO_2-ETL and PANDI SAM at (a) room temperature storage and (b) 65 °C under nitrogen and dark conditions.

associated with more efficient charge extraction/transport at the ITO/SAM/perovskite interface.[31,65]

On the other hand, Figure 5f shows the V_{OC} with respect to light intensity to determine the diode ideality factor of the PSCs. The diode ideality factor was calculated following $n_{id} = \frac{q}{K_B T} \times \frac{dV_{OC}}{d \ln \theta}$, where kT/q is the thermal voltage and can be extracted from the slope of the V_{OC} as a function of the light intensity.[66] The slope for SnO_2 devices shows a higher value ($\sim$1.62 $k_B T/q$) than that of **PANDI**-based ($\sim$1.32 $k_B T/q$) devices. Thus, the larger slope value, the greater the probability of trap-assisted recombination. The reduced ideality factor of PSCs with SAM compared to those with SnO_2 indicated suppressed trap-assisted bimolecular recombination at the electron-selective interface.[67,68]

Finally, we also evaluated the long-term stability of the *n-i-p* devices. First, we stored the devices based on SnO_2-ETL and **PANDI** SAM inside a N_2-filled glovebox at room temperature for 1000 h and measured the devices regularly (Figure 6a). The SnO_2-based *n-i-p* devices could only retain around 58% of their initial PCEs after 1000 h of storage (in accordance with previous reports), while the **PANDI** SAM-based devices showed at 84% a much superior retention.[69,70] Next, we also evaluated the thermal stability of our devices kept on a hot plate at 65 °C in a N_2-filled glovebox in the dark for more than 1000 h and compared **PANDI** SAM and SnO_2-based devices in Figure 6b. This clearly showed that **PANDI** SAM-based devices demonstrated a better thermal stability, with around 72% retention of their initial PCEs, compared to SnO_2-based devices with only 38% retention under identical conditions. The functional head group of **PANDI** consists of two methyl groups exhibiting a strong interaction to the PbI_6 framework in the perovskite, increasing the energy barrier for halide migration to the ETL bottom interface.[71] It should be noted that the degradation of *n-i-p* devices can also be initiated due to use of doped spiro-OMeTAD as an HTL under elevated temperature.[2,17,72−76] For this reason, we also evaluated our **PANDI** SAM-based devices employing poly[bis(4-phenyl)-(2,4,6-trimethylphenyl)amine] (PTAA), a more thermally stable HTL, with devices showing above 90% retention of their performance under identical conditions. In addition, the ITO-SnO_2/perovskite interface also clearly further induced degradation due to redox reactions and charge accumulation during the stability tests, whereas these effects can be minimized with the use of organic SAM/perovskite interfaces.[8,45,61,77−79]

In summary, **PANDI** and **PAAQ** SAMs were successfully synthesized and investigated as electron-selective bottom contacts for *n-i-p* PSC. Both SAM molecules show a sufficient thermal stability and relatively suitable energetic alignment with the perovskite absorber and ITO contact. In particular, **PANDI**-based SAMs demonstrate a higher surface homogeneity on the ITO surface than **PAAQ** SAMs. We found that the increasing surface homogeneity on the ITO/**PANDI** can effectively suppress nonradiative interfacial recombination through the field-effect passivation, as indicated by longer charge carrier lifetimes and higher QFLS values. We also performed trSPV measurements and charge transport modeling, showing sufficient electron extraction and a relatively lower defect density at the ITO/**PANDI**/perovskite interface. Notably, the ITO/**PANDI** interface offers multiple benefits of lower optical reflectance and interfacial energetic losses, simultaneously, compared to the conventionally used SnO_2 ETL. As a result, ITO/**PANDI**-based *n-i-p* PSCs demonstrate a champion PCE of around 21.5%, representing the highest PCE among organic ETLs based on reported *n-i-p* PSCs, so far. Additionally, our PANDI SAMs also show the capability to be applied to flexible substrates. Finally, the **PANDI**-based device also showed improved operational long-term thermal stability, confirming that the **PANDI** SAM has a potential future to be utilized as ETL materials.

■ ASSOCIATED CONTENT

Supporting Information

The Supporting Information is available free of charge at https://pubs.acs.org/doi/10.1021/acsenergylett.4c00306.

Detailed experimental and characterization method, synthesis route, molecular NMR results, cyclic voltammetry and thermogravimetric measurements, SAM UV−vis spectra, Kelvin probe measurements, ITO/SAM topographic atomic microscopy, XPS analysis, surface water contact angle, cross-sectional SEM, steady-state PL and time-resolved PL, summary of photovoltaic parameters of various organic ETLs and ETL-Free for *n-i-p* devices, device statistics, $J-V$ performance for SnO_2 and flexible devices, and transient surface photovoltage fitting method (PDF)

■ AUTHOR INFORMATION

Corresponding Authors

Artem Musiienko − *Solar Energy Division, Helmholtz-Zentrum Berlin für Materialien und Energie GmbH, 12489*

https://doi.org/10.1021/acsenergylett.4c00306
ACS Energy Lett. 2024, 9, 1682−1692

Berlin, Germany; Email: artem.musiienko@helmholtz-berlin.de

Randi Azmi − *KAUST Solar Center (KSC), Physical and Engineering Division (PSE), King Abdullah University of Science and Technology (KAUST), Thuwal 23955-6900, Kingdom of Saudi Arabia*; Email: randi.azmi@kaust.edu.sa

Tadas Malinauskas − *Department of Organic Chemistry, Kaunas University of Technology, Kaunas 50254, Lithuania*; orcid.org/0000-0002-5478-6550; Email: tadas.malinauskas@ktu.lt

Stefaan De Wolf − *KAUST Solar Center (KSC), Physical and Engineering Division (PSE), King Abdullah University of Science and Technology (KAUST), Thuwal 23955-6900, Kingdom of Saudi Arabia*; orcid.org/0000-0003-1619-9061; Email: stefaan.dewolf@kaust.edu.sa

Authors

Drajad S. Utomo − *KAUST Solar Center (KSC), Physical and Engineering Division (PSE), King Abdullah University of Science and Technology (KAUST), Thuwal 23955-6900, Kingdom of Saudi Arabia; Material Science and Engineering (MSE), Physical and Engineering Division (PSE), King Abdullah University of Science and Technology (KAUST), Thuwal 23955-6900, Kingdom of Saudi Arabia*

Lauryna M. Svirskaite − *Department of Organic Chemistry, Kaunas University of Technology, Kaunas 50254, Lithuania*

Adi Prasetio − *KAUST Solar Center (KSC), Physical and Engineering Division (PSE), King Abdullah University of Science and Technology (KAUST), Thuwal 23955-6900, Kingdom of Saudi Arabia; Material Science and Engineering (MSE), Physical and Engineering Division (PSE), King Abdullah University of Science and Technology (KAUST), Thuwal 23955-6900, Kingdom of Saudi Arabia*

Vida Malinauskiene − *Department of Organic Chemistry, Kaunas University of Technology, Kaunas 50254, Lithuania*

Pia Dally − *KAUST Solar Center (KSC), Physical and Engineering Division (PSE), King Abdullah University of Science and Technology (KAUST), Thuwal 23955-6900, Kingdom of Saudi Arabia*

Erkan Aydin − *KAUST Solar Center (KSC), Physical and Engineering Division (PSE), King Abdullah University of Science and Technology (KAUST), Thuwal 23955-6900, Kingdom of Saudi Arabia*; orcid.org/0000-0002-8849-2788

Vytautas Getautis − *Department of Organic Chemistry, Kaunas University of Technology, Kaunas 50254, Lithuania*; orcid.org/0000-0001-7695-4677

Complete contact information is available at: https://pubs.acs.org/10.1021/acsenergylett.4c00306

Author Contributions

[⊥]D.S.U. and L.M.S. contributed equally to this work.

Author Contributions

D.S.U. and R.A. fabricated and did characterizations of perovskite samples and devices. L.M.S. and V.M. synthesized the SAMs and performed NMR measurements. L.M.S. performed TGA and CV measurements. D.S.U. performed SEM, hyperspectral photoluminescence, and UV−vis measurements. A.P. conducted the SKPM and AFM measurements and did analysis. P.D. performed XPS and did data analysis. A.M. conducted the trSPV measurements and analysis. R.A. and T.M. conceived the idea and wrote the original manuscript. R.A., D.S.U., L.M.S., T.M., A.M., E.A., and S.D.W. contributed to reviewing and writing to the manuscript. R.A., T.M., V.G., and S.D.W. supervised the project. S.D.W. secured the funding. All authors contributed to the manuscript.

Notes

The authors declare no competing financial interest.

■ ACKNOWLEDGMENTS

We thank Rakesh R. Pradhan for help in discussions clarifying dipole moment calculation. This work was supported by the King Abdullah University of Science and Technology (KAUST) Office of Sponsored Research (OSR) under contract numbers OSR-CRG2020-4350, ORA-CRG2021-4669, and ORFS-CRG11-2022-5035. This study was in part also funded by the European Union. Views and opinions expressed are however those of the author(s) only and do not necessarily reflect those of the European Union or CINEA. Neither the European Union nor the granting authority can be held responsible for them. VALHALLA project has received funding from Horizon Europe Research and Innovation Action programme under Grant Agreement no. 101082176. L.M.S., T.M., K.R., and V.G. acknowledge the funding from the Research Council of Lithuania (LMTLT), agreement no. S-A-UEI-23-1 (22-12-2023).

■ REFERENCES

(1) Al-Ashouri, A.; Magomedov, A.; Ross, M.; Jost, M.; Talaikis, M.; Chistiakova, G.; Bertram, T.; Márquez, J. A.; Köhnen, E.; Kasparavicius, E.; et al. Conformal monolayer contacts with lossless interfaces for perovskite single junction and monolithic tandem solar cells. *Energy Environ. Sci.* **2019**, *12* (11), 3356−3369.

(2) Yao, Y.; Cheng, C.; Zhang, C.; Hu, H.; Wang, K.; De Wolf, S. Organic Hole-Transport Layers for Efficient, Stable, and Scalable Inverted Perovskite Solar Cells. *Adv. Mater.* **2022**, *34* (44), 2203794.

(3) Tan, Q.; Li, Z.; Luo, G.; Zhang, X.; Che, B.; Chen, G.; Gao, H.; He, D.; Ma, G.; Wang, J.; et al. Inverted perovskite solar cells using dimethylacridine-based dopants. *Nature* **2023**, *620*, 545.

(4) Zhang, S.; Ye, F.; Wang, X.; Chen, R.; Zhang, H.; Zhan, L.; Jiang, X.; Li, Y.; Ji, X.; Liu, S.; et al. Minimizing buried interfacial defects for efficient inverted perovskite solar cells. *Science* **2023**, *380* (6643), 404−409.

(5) Liang, Z.; Zhang, Y.; Xu, H.; Chen, W.; Liu, B.; Zhang, J.; Zhang, H.; Wang, Z.; Kang, D.-H.; Zeng, J.; et al. Out-of-plane cations homogenise perovskite composition for solar cells. *Nature* **2023**, *624*, 557.

(6) Azmi, R.; Utomo, D. S.; Vishal, B.; Zhumagali, S.; Dally, P.; Risqi, A. M.; Prasetio, A.; Ugur, E.; Cao, F.; Imran, I. F.; et al. Double-side 2-dimensional/3-dimensional heterojunctions for inverted perovskite solar cells. *Nature* **2024**, DOI: 10.1038/s41586-024-07189-3.

(7) Al-Ashouri, A.; Köhnen, E.; Li, B.; Magomedov, A.; Hempel, H.; Caprioglio, P.; Márquez, J. A.; Morales Vilches, A. B.; Kasparavicius, E.; Smith, J. A.; et al. Monolithic perovskite/silicon tandem solar cell with > 29% efficiency by enhanced hole extraction. *Science* **2020**, *370* (6522), 1300−1309.

(8) Levine, I.; Al-Ashouri, A.; Musiienko, A.; Hempel, H.; Magomedov, A.; Drevilkauskaite, A.; Getautis, V.; Menzel, D.; Hinrichs, K.; Unold, T.; et al. Charge transfer rates and electron trapping at buried interfaces of perovskite solar cells. *Joule* **2021**, *5* (11), 2915−2933.

(9) Azmi, R.; Ugur, E.; Seitkhan, A.; Aljamaan, F.; Subbiah, A. S.; Liu, J.; Harrison, G. T.; Nugraha, M. I.; Eswaran, M. K.; Babics, M.; et al. Damp heat-stable perovskite solar cells with tailored-dimensionality 2D/3D heterojunctions. *Science* **2022**, *376* (6588), 73−77.

(10) Liu, J.; De Bastiani, M.; Aydin, E.; Harrison, G. T.; Gao, Y.; Pradhan, R. R.; Eswaran, M. K.; Mandal, M.; Yan, W.; Seitkhan, A.;

et al. Efficient and stable perovskite-silicon tandem solar cells through contact displacement by MgFx. *Science* **2022**, *377* (6603), 302−306.
(11) Best Research-Cell Efficiency Chart (NREL). https://www.nrel.gov/pv/interactive-cell-efficiency.html. (acccessed 20th Desember 2023; 20:18:51).
(12) Aydin, E.; Ugur, E.; Yildirim, B. K.; Allen, T. G.; Dally, P.; Razzaq, A.; Cao, F.; Xu, L.; Vishal, B.; Yazmaciyan, A.; et al. Enhanced optoelectronic coupling for perovskite-silicon tandem solar cells. *Nature* **2023**, *623*, 732.
(13) Tan, Q.; Li, Z.; Luo, G.; Zhang, X.; Che, B.; Chen, G.; Gao, H.; He, D.; Ma, G.; Wang, J.; et al. Inverted perovskite solar cells using dimethylacridine-based dopants. *Nature* **2023**, *620* (7974), 545−551.
(14) Wang, Y.-C.; Li, X.; Zhu, L.; Liu, X.; Zhang, W.; Fang, J. Efficient and Hysteresis-Free Perovskite Solar Cells Based on a Solution Processable Polar Fullerene Electron Transport Layer. *Adv. Energy Mater.* **2017**, *7* (21), 1701144.
(15) Li, L.; Wu, Y.; Li, E.; Shen, C.; Zhang, H.; Xu, X.; Wu, G.; Cai, M.; Zhu, W.-H. Self-assembled naphthalimide derivatives as an efficient and low-cost electron extraction layer for n-i-p perovskite solar cells. *Chem. Commun.* **2019**, *55* (88), 13239−13242.
(16) Meng, D.; Xue, J.; Zhao, Y.; Zhang, E.; Zheng, R.; Yang, Y. Configurable Organic Charge Carriers toward Stable Perovskite Photovoltaics. *Chem. Rev.* **2022**, *122* (18), 14954−14986.
(17) Azmi, R.; Zhumagali, S.; Bristow, H.; Zhang, S.; Yazmaciyan, A.; Pininti, A. R.; Utomo, D. S.; Subbiah, A. S.; De Wolf, S. Moisture-Resilient Perovskite Solar Cells for Enhanced Stability. *Adv. Mater.* **2023**, 2211317.
(18) Nielsen, C. B.; Holliday, S.; Chen, H.-Y.; Cryer, S. J.; McCulloch, I. Non-Fullerene Electron Acceptors for Use in Organic Solar Cells. *Acc. Chem. Res.* **2015**, *48* (11), 2803−2812.
(19) Aydin, E.; Liu, J.; Ugur, E.; Azmi, R.; Harrison, G. T.; Hou, Y.; Chen, B.; Zhumagali, S.; De Bastiani, M.; Wang, M.; et al. Ligand-bridged charge extraction and enhanced quantum efficiency enable efficient n-i-p perovskite/silicon tandem solar cells. *Energy Environ. Sci.* **2021**, *14* (8), 4377−4390.
(20) De Bastiani, M.; Armaroli, G.; Jalmood, R.; Ferlauto, L.; Li, X.; Tao, R.; Harrison, G. T.; Eswaran, M. K.; Azmi, R.; Babics, M.; et al. Mechanical Reliability of Fullerene/Tin Oxide Interfaces in Monolithic Perovskite/Silicon Tandem Cells. *ACS Energy Letters* **2022**, *7* (2), 827−833.
(21) Jung, S.-K.; Heo, J. H.; Lee, D. W.; Lee, S.-C.; Lee, S.-H.; Yoon, W.; Yun, H.; Im, S. H.; Kim, J. H.; Kwon, O.-P. Nonfullerene Electron Transporting Material Based on Naphthalene Diimide Small Molecule for Highly Stable Perovskite Solar Cells with Efficiency Exceeding 20%. *Adv. Funct. Mater.* **2018**, *28* (20), 1800346.
(22) Jameel, M. A.; Yang, T. C.-J.; Wilson, G. J.; Evans, R. A.; Gupta, A.; Langford, S. J. Naphthalene diimide-based electron transport materials for perovskite solar cells. *Journal of Materials Chemistry A* **2021**, *9* (48), 27170−27192.
(23) Said, A. A.; Wagalgave, S. M.; Xie, J.; Puyad, A. L.; Chen, W.; Wang, Z.; Bhosale, S. V.; Bhosale, S. V.; Zhang, Q. NDI-based small molecules as electron transporting layers in solution-processed planar perovskite solar cells. *J. Solid State Chem.* **2019**, *270*, 51−57.
(24) Said, A. A.; Xie, J.; Zhang, Q. Recent Progress in Organic Electron Transport Materials in Inverted Perovskite Solar Cells. *Small* **2019**, *15* (27), 1900854.
(25) Valero, S.; Cabrera-Espinoza, A.; Collavini, S.; Pascual, J.; Marinova, N.; Kosta, I.; Delgado, J. L. Naphthalene Diimide-Based Molecules for Efficient and Stable Perovskite Solar Cells. *Eur. J. Org. Chem.* **2020**, *2020* (33), 5329−5339.
(26) Peng, S.; Miao, J.; Murtaza, I.; Zhao, L.; Hu, Z.; Liu, M.; Yang, T.; Liang, Y.; Meng, H.; Huang, W. An efficient and thickness insensitive cathode interface material for high performance inverted perovskite solar cells with 17.27% efficiency. *Journal of Materials Chemistry C* **2017**, *5* (24), 5949−5955.
(27) Altinkaya, C.; Aydin, E.; Ugur, E.; Isikgor, F. H.; Subbiah, A. S.; De Bastiani, M.; Liu, J.; Babayigit, A.; Allen, T. G.; Laquai, F.; et al. Tin Oxide Electron-Selective Layers for Efficient, Stable, and Scalable Perovskite Solar Cells. *Adv. Mater.* **2021**, *33* (15), 2005504.
(28) Yu, R.; Wei, X.; Wu, G.; Zhang, T.; Gong, Y.; Zhao, B.; Hou, J.; Yang, C.; Tan, Z. a. Efficient interface modification via multi-site coordination for improved efficiency and stability in organic solar cells. *Energy Environ. Sci.* **2022**, *15* (2), 822−829.
(29) Kim, W.; Ahmad, Z.; Lee, H.-J.; Yoo, S. J.; Shim, J.-J.; Lee, J.-S. Electrochemical properties of anthraquinone-containing polymer nanocomposite by nano-level molecular ordering. *Polym. Chem.* **2021**, *12* (42), 6154−6160.
(30) Li, S.; Fu, Q.; Meng, L.; Wan, X.; Ding, L.; Lu, G.; Lu, G.; Yao, Z.; Li, C.; Chen, Y. Achieving over 18% Efficiency Organic Solar Cell Enabled by a ZnO-Based Hybrid Electron Transport Layer with an Operational Lifetime up to 5 Years. *Angew. Chem., Int. Ed.* **2022**, *61* (34), No. e202207397.
(31) Azmi, R.; Hwang, S.; Yin, W.; Kim, T.-W.; Ahn, T. K.; Jang, S.-Y. High Efficiency Low-Temperature Processed Perovskite Solar Cells Integrated with Alkali Metal Doped ZnO Electron Transport Layers. *ACS Energy Letters* **2018**, *3* (6), 1241−1246.
(32) Bu, T.; Li, J.; Zheng, F.; Chen, W.; Wen, X.; Ku, Z.; Peng, Y.; Zhong, J.; Cheng, Y.-B.; Huang, F. Universal passivation strategy to slot-die printed SnO2 for hysteresis-free efficient flexible perovskite solar module. *Nat. Commun.* **2018**, *9* (1), 4609.
(33) Park, S. Y.; Zhu, K. Advances in SnO2 for Efficient and Stable n-i-p Perovskite Solar Cells. *Adv. Mater.* **2022**, *34* (27), 2110438.
(34) Tan, H.; Jain, A.; Voznyy, O.; Lan, X.; García de Arquer, F. P.; Fan, J. Z.; Quintero-Bermudez, R.; Yuan, M.; Zhang, B.; Zhao, Y.; et al. Efficient and stable solution-processed planar perovskite solar cells via contact passivation. *Science* **2017**, *355* (6326), 722−726.
(35) Xiong, Z.; Chen, X.; Zhang, B.; Odunmbaku, G. O.; Ou, Z.; Guo, B.; Yang, K.; Kan, Z.; Lu, S.; Chen, S.; et al. Simultaneous Interfacial Modification and Crystallization Control by Biguanide Hydrochloride for Stable Perovskite Solar Cells with PCE of 24.4%. *Adv. Mater.* **2022**, *34* (8), 2106118.
(36) Prasetio, A.; Pradhan, R. R.; Dally, P.; Ghadiyali, M.; Azmi, R.; Schwingenschlögl, U.; Allen, T. G.; De Wolf, S. Efficient Silicon Solar Cells through Organic Self-Assembled Monolayers as Electron Selective Contacts. *Adv. Energy Mater.* **2023**, *14*, 2303705.
(37) Ali, F.; Roldán-Carmona, C.; Sohail, M.; Nazeeruddin, M. K. Applications of Self-Assembled Monolayers for Perovskite Solar Cells Interface Engineering to Address Efficiency and Stability. *Adv. Energy Mater.* **2020**, *10* (48), 2002989.
(38) Diez-Cabanes, V.; Morales, D. C.; Souto, M.; Paradinas, M.; Delchiaro, F.; Painelli, A.; Ocal, C.; Cornil, D.; Cornil, J.; Veciana, J.; et al. Effect of the Molecular Polarizability of SAMs on the Work Function Modification of Gold: Closed- versus Open-Shell Donor-Acceptor SAMs. *Advanced Materials Technologies* **2019**, *4* (5), 1800152.
(39) Azmi, R.; Hadmojo, W. T.; Sinaga, S.; Lee, C.-L.; Yoon, S. C.; Jung, I. H.; Jang, S.-Y. High-Efficiency Low-Temperature ZnO Based Perovskite Solar Cells Based on Highly Polar, Nonwetting Self-Assembled Molecular Layers. *Adv. Energy Mater.* **2018**, *8* (5), 1701683.
(40) Azmi, R.; Nam, S. Y.; Sinaga, S.; Oh, S.-H.; Ahn, T. K.; Yoon, S. C.; Jung, I. H.; Jang, S.-Y. Improved performance of colloidal quantum dot solar cells using high-electric-dipole self-assembled layers. *Nano Energy* **2017**, *39*, 355−362.
(41) Chen, Q.; Wang, C.; Li, Y.; Chen, L. Interfacial Dipole in Organic and Perovskite Solar Cells. *J. Am. Chem. Soc.* **2020**, *142* (43), 18281−18292.
(42) Prasetio, A.; Pradhan, R. R.; Dally, P.; Ghadiyali, M.; Azmi, R.; Schwingenschlögl, U.; Allen, T. G.; De Wolf, S. Efficient Silicon Solar Cells through Organic Self-Assembled Monolayers as Electron Selective Contacts. *Adv. Energy Mater.* **2024**, *14*, 2303705.
(43) Deng, X.; Qi, F.; Li, F.; Wu, S.; Lin, F. R.; Zhang, Z.; Guan, Z.; Yang, Z.; Lee, C.-S.; Jen, A. K.-Y. Co-assembled Monolayers as Hole-Selective Contact for High-Performance Inverted Perovskite Solar Cells with Optimized Recombination Loss and Long-Term Stability. *Angew. Chem., Int. Ed.* **2022**, *61* (30), No. e202203088.
(44) Bi, C.; Wang, Q.; Shao, Y.; Yuan, Y.; Xiao, Z.; Huang, J. Non-wetting surface-driven high-aspect-ratio crystalline grain growth for

efficient hybrid perovskite solar cells. *Nat. Commun.* **2015**, *6* (1), 7747.
(45) Azmi, R.; Lee, C.-L.; Jung, I. H.; Jang, S.-Y. Simultaneous Improvement in Efficiency and Stability of Low-Temperature-Processed Perovskite Solar Cells by Interfacial Control. *Adv. Energy Mater.* **2018**, *8* (14), 1702934.
(46) Warby, J.; Zu, F.; Zeiske, S.; Gutierrez-Partida, E.; Frohloff, L.; Kahmann, S.; Frohna, K.; Mosconi, E.; Radicchi, E.; Lang, F.; et al. Understanding Performance Limiting Interfacial Recombination in pin Perovskite Solar Cells. *Adv. Energy Mater.* **2022**, *12* (12), 2103567.
(47) Andaji-Garmaroudi, Z.; Abdi-Jalebi, M.; Guo, D.; Macpherson, S.; Sadhanala, A.; Tennyson, E. M.; Ruggeri, E.; Anaya, M.; Galkowski, K.; Shivanna, R.; et al. A Highly Emissive Surface Layer in Mixed-Halide Multication Perovskites. *Adv. Mater.* **2019**, *31* (42), 1902374.
(48) Gaury, B.; Haney, P. M. Probing surface recombination velocities in semiconductors using two-photon microscopy. *J. Appl. Phys.* **2016**, *119* (12), 125105.
(49) Iqbal, Z.; Zu, F.; Musiienko, A.; Gutierrez-Partida, E.; Köbler, H.; Gries, T. W.; Sannino, G. V.; Canil, L.; Koch, N.; Stolterfoht, M.; et al. Interface Modification for Energy Level Alignment and Charge Extraction in CsPbI3 Perovskite Solar Cells. *ACS Energy Letters* **2023**, *8* (10), 4304−4314.
(50) Magomedov, A.; Al-Ashouri, A.; Kasparavičius, E.; Strazdaite, S.; Niaura, G.; Jošt, M.; Malinauskas, T.; Albrecht, S.; Getautis, V. Self-Assembled Hole Transporting Monolayer for Highly Efficient Perovskite Solar Cells. *Adv. Energy Mater.* **2018**, *8* (32), 1801892.
(51) Mariotti, S.; Köhnen, E.; Scheler, F.; Sveinbjörnsson, K.; Zimmermann, L.; Piot, M.; Yang, F.; Li, B.; Warby, J.; Musiienko, A.; et al. Interface engineering for high-performance, triple-halide perovskite-silicon tandem solar cells. *Science* **2023**, *381* (6653), 63−69.
(52) Musiienko, A.; Yang, F.; Gries, T. W.; Frasca, C.; Friedrich, D.; Al-Ashouri, A.; Sağlamkaya, E.; Lang, F.; Kojda, D.; Huang, Y.-T.; et al. Resolving electron and hole transport properties in semiconductor materials by constant light-induced magneto transport. *Nat. Commun.* **2024**, *15* (1), 316.
(53) Liu, D.; Yang, J.; Kelly, T. L. Compact Layer Free Perovskite Solar Cells with 13.5% Efficiency. *J. Am. Chem. Soc.* **2014**, *136* (49), 17116−17122.
(54) Zhumagali, S.; Isikgor, F. H.; Maity, P.; Yin, J.; Ugur, E.; De Bastiani, M.; Subbiah, A. S.; Mirabelli, A. J.; Azmi, R.; Harrison, G. T.; et al. Linked Nickel Oxide/Perovskite Interface Passivation for High-Performance Textured Monolithic Tandem Solar Cells. *Adv. Energy Mater.* **2021**, *11* (40), 2101662.
(55) Ke, W.; Fang, G.; Liu, Q.; Xiong, L.; Qin, P.; Tao, H.; Wang, J.; Lei, H.; Li, B.; Wan, J.; et al. Low-Temperature Solution-Processed Tin Oxide as an Alternative Electron Transporting Layer for Efficient Perovskite Solar Cells. *J. Am. Chem. Soc.* **2015**, *137* (21), 6730−6733.
(56) Meng, L.; Sun, C.; Wang, R.; Huang, W.; Zhao, Z.; Sun, P.; Huang, T.; Xue, J.; Lee, J.-W.; Zhu, C.; et al. Tailored Phase Conversion under Conjugated Polymer Enables Thermally Stable Perovskite Solar Cells with Efficiency Exceeding 21%. *J. Am. Chem. Soc.* **2018**, *140* (49), 17255−17262.
(57) Kokaba, M. R.; Ahmed, Y.; Yeddu, V.; Zhang, D.; Moazzezi, P.; Kamraninejad, V.; Dayneko, S.; Reinecke, S. B.; Amaro, A.; Villarejo, B. Enhanced Particle-to-Particle Interaction of Tin Oxide Electron Transporter Layer for Scalable Flexible Perovskite Solar Cells. *Solar RRL* **2024**, 2301013.
(58) Li, X.; Yu, H.; Liu, Z.; Huang, J.; Ma, X.; Liu, Y.; Sun, Q.; Dai, L.; Ahmad, S.; Shen, Y.; et al. Progress and Challenges Toward Effective Flexible Perovskite Solar Cells. *Nano-Micro Letters* **2023**, *15* (1), 206.
(59) Ugur, E.; Aydin, E.; De Bastiani, M.; Harrison, G. T.; Yildirim, B. K.; Teale, S.; Chen, B.; Liu, J.; Wang, M.; Seitkhan, A.; et al. Front-contact passivation through 2D/3D perovskite heterojunctions enables efficient bifacial perovskite/silicon tandem solar cells. *Matter* **2023**, *6* (9), 2919−2934.
(60) Ahmadi, M.; Hsiao, Y.-C.; Wu, T.; Liu, Q.; Qin, W.; Hu, B. Effect of Photogenerated Dipoles in the Hole Transport Layer on Photovoltaic Performance of Organic-Inorganic Perovskite Solar Cells. *Adv. Energy Mater.* **2017**, *7* (4), 1601575.
(61) Azmi, R.; Nurrosyid, N.; Lee, S.-H.; Al Mubarok, M.; Lee, W.; Hwang, S.; Yin, W.; Ahn, T. K.; Kim, T.-W.; Ryu, D. Y.; et al. Shallow and Deep Trap State Passivation for Low-Temperature Processed Perovskite Solar Cells. *ACS Energy Letters* **2020**, *5* (5), 1396−1403.
(62) Ansari, F.; Shirzadi, E.; Salavati-Niasari, M.; LaGrange, T.; Nonomura, K.; Yum, J.-H.; Sivula, K.; Zakeeruddin, S. M.; Nazeeruddin, M. K.; Grätzel, M.; et al. Passivation Mechanism Exploiting Surface Dipoles Affords High-Performance Perovskite Solar Cells. *J. Am. Chem. Soc.* **2020**, *142* (26), 11428−11433.
(63) Zuo, L.; Gu, Z.; Ye, T.; Fu, W.; Wu, G.; Li, H.; Chen, H. Enhanced Photovoltaic Performance of CH3NH3PbI3 Perovskite Solar Cells through Interfacial Engineering Using Self-Assembling Monolayer. *J. Am. Chem. Soc.* **2015**, *137* (7), 2674−2679.
(64) Wang, J.; Li, J.; Zhou, Y.; Yu, C.; Hua, Y.; Yu, Y.; Li, R.; Lin, X.; Chen, R.; Wu, H.; et al. Tuning an Electrode Work Function Using Organometallic Complexes in Inverted Perovskite Solar Cells. *J. Am. Chem. Soc.* **2021**, *143* (20), 7759−7768.
(65) Liu, L.; Mei, A.; Liu, T.; Jiang, P.; Sheng, Y.; Zhang, L.; Han, H. Fully Printable Mesoscopic Perovskite Solar Cells with Organic Silane Self-Assembled Monolayer. *J. Am. Chem. Soc.* **2015**, *137* (5), 1790−1793.
(66) Glowienka, D.; Galagan, Y. Light Intensity Analysis of Photovoltaic Parameters for Perovskite Solar Cells. *Adv. Mater.* **2022**, *34* (2), 2105920.
(67) Bai, S.; Jin, Y.; Liang, X.; Ye, Z.; Wu, Z.; Sun, B.; Ma, Z.; Tang, Z.; Wang, J.; Würfel, U.; et al. Ethanedithiol Treatment of Solution-Processed ZnO Thin Films: Controlling the Intragap States of Electron Transporting Interlayers for Efficient and Stable Inverted Organic Photovoltaics. *Adv. Energy Mater.* **2015**, *5* (5), 1401606.
(68) Azmi, R.; Oh, S.-H.; Jang, S.-Y. High-Efficiency Colloidal Quantum Dot Photovoltaic Devices Using Chemically Modified Heterojunctions. *ACS Energy Letters* **2016**, *1* (1), 100−106.
(69) Liu, Z.; Qiu, L.; Ono, L. K.; He, S.; Hu, Z.; Jiang, M.; Tong, G.; Wu, Z.; Jiang, Y.; Son, D.-Y.; et al. A holistic approach to interface stabilization for efficient perovskite solar modules with over 2,000-h operational stability. *Nature Energy* **2020**, *5* (8), 596−604.
(70) Luo, T.; Ye, G.; Chen, X.; Wu, H.; Zhang, W.; Chang, H. F-doping-Enhanced Carrier Transport in the SnO2/Perovskite Interface for High-Performance Perovskite Solar Cells. *ACS Appl. Mater. Interfaces* **2022**, *14* (37), 42093−42101.
(71) Guo, H.; Wang, X.; Li, C.; Hu, H.; Zhang, H.; Zhang, L.; Zhu, W.-H.; Wu, Y. Immobilizing Surface Halide in Perovskite Solar Cells via Calix[4]pyrrole. *Adv. Mater.* **2023**, *35* (26), 2301871.
(72) Azmi, R.; Nam, S. Y.; Sinaga, S.; Akbar, Z. A.; Lee, C.-L.; Yoon, S. C.; Jung, I. H.; Jang, S.-Y. High-performance dopant-free conjugated small molecule-based hole-transport materials for perovskite solar cells. *Nano Energy* **2018**, *44*, 191−198.
(73) Liu, X.; Zheng, B.; Shi, L.; Zhou, S.; Xu, J.; Liu, Z.; Yun, J. S.; Choi, E.; Zhang, M.; Lv, Y.; et al. Perovskite solar cells based on spiro-OMeTAD stabilized with an alkylthiol additive. *Nat. Photonics* **2023**, *17* (1), 96−105.
(74) Fu, Q.; Tang, X.; Liu, H.; Wang, R.; Liu, T.; Wu, Z.; Woo, H. Y.; Zhou, T.; Wan, X.; Chen, Y.; et al. Ionic Dopant-Free Polymer Alloy Hole Transport Materials for High-Performance Perovskite Solar Cells. *J. Am. Chem. Soc.* **2022**, *144* (21), 9500−9509.
(75) Wang, S.; Huang, Z.; Wang, X.; Li, Y.; Günther, M.; Valenzuela, S.; Parikh, P.; Cabreros, A.; Xiong, W.; Meng, Y. S. Unveiling the Role of tBP-LiTFSI Complexes in Perovskite Solar Cells. *J. Am. Chem. Soc.* **2018**, *140* (48), 16720−16730.
(76) Zhang, F.; Yao, Z.; Guo, Y.; Li, Y.; Bergstrand, J.; Brett, C. J.; Cai, B.; Hajian, A.; Guo, Y.; Yang, X.; et al. Polymeric, Cost-Effective, Dopant-Free Hole Transport Materials for Efficient and Stable Perovskite Solar Cells. *J. Am. Chem. Soc.* **2019**, *141* (50), 19700−19707.

https://doi.org/10.1021/acsenergylett.4c00306
ACS Energy Lett. 2024, 9, 1682−1692

(77) Boyd, C. C.; Shallcross, R. C.; Moot, T.; Kerner, R.; Bertoluzzi, L.; Onno, A.; Kavadiya, S.; Chosy, C.; Wolf, E. J.; Werner, J.; et al. Overcoming Redox Reactions at Perovskite-Nickel Oxide Interfaces to Boost Voltages in Perovskite Solar Cells. *Joule* **2020**, *4* (8), 1759−1775.
(78) Liang, J.-W.; Firdaus, Y.; Azmi, R.; Faber, H.; Kaltsas, D.; Kang, C. H.; Nugraha, M. I.; Yengel, E.; Ng, T. K.; De Wolf, S.; et al. Cl2-Doped CuSCN Hole Transport Layer for Organic and Perovskite Solar Cells with Improved Stability. *ACS Energy Letters* **2022**, *7* (9), 3139−3148.
(79) Shao, Y.; Xiao, Z.; Bi, C.; Yuan, Y.; Huang, J. Origin and elimination of photocurrent hysteresis by fullerene passivation in CH3NH3PbI3 planar heterojunction solar cells. *Nat. Commun.* **2014**, *5* (1), 5784.

https://doi.org/10.1021/acsenergylett.4c00306
ACS Energy Lett. 2024, 9, 1682−1692